

# Reversible Formation of 2D Electron Gas at the LaFeO<sub>3</sub>/SrTiO<sub>3</sub> Interface via Control of Oxygen Vacancies

Pengfa Xu, Wei Han, Philip M. Rice, Jaewoo Jeong, Mahesh G. Samant, Katayoon Mohseni, Holger L. Meyerheim, Sergey Ostanin, Igor V. Maznichenko, Ingrid Mertig, Eberhard K. U. Gross, Arthur Ernst, and Stuart S. P. Parkin\*

The controlled metallization of insulators underlies many current and future technologies. Metallization of a wide variety of insulating materials can be accomplished in various ways including by chemical or electrostatic doping, or via pressure, temperature, or strain.<sup>[1–3]</sup> One especially interesting class of materials that has attracted much attention is the combination of polar<sup>[4]</sup> and nonpolar insulating oxides.<sup>[5–7]</sup> The interface between these oxides is sometimes found to be metallic in the form of a 2D electron gas (2DEG). The archetypal pair is SrTiO<sub>3</sub>/LaAlO<sub>3</sub> (STO/LAO)<sup>[8–11]</sup> for which a theory based on a “polar catastrophe” of an increasing electric field with thickness of the polar LAO layer results in charge transfer from the LAO surface to the interface to form the 2DEG in ideal systems.<sup>[12]</sup> Several other heterojunctions between nominally insulating STO and various polar insulating oxides have been shown to be conducting, including, for example, LaVO<sub>3</sub>/STO,<sup>[13]</sup> LaGaO<sub>3</sub>/STO,<sup>[14]</sup> GdTlO<sub>3</sub>/STO,<sup>[15]</sup> LaTiO<sub>3</sub>/STO,<sup>[16]</sup> and SmTiO<sub>3</sub>/STO.<sup>[17]</sup> In many of these systems it is difficult to rule out possible deviations from the ideal structure that can include, for example, cation intermixing<sup>[18]</sup> or oxygen off-stoichiometry.<sup>[19–23]</sup> The role of such imperfections is complex. Here, we consider heterojunctions formed from LaFeO<sub>3</sub> (LFO) and STO since LFO has one of the highest known antiferromagnetic ordering temperatures,<sup>[24]</sup> and, moreover, is almost perfectly lattice matched with STO (the LFO lattice is only 0.53% larger than that of STO). One of the motivations for this study is to explore potential superconductivity in thin films of LFO in which, via finite size scaling effects, the Néel temperature is suppressed while short-range magnetic order is maintained. We have found that the

Néel temperature of even three unit cell (u.c.) thick LFO films remains well above room temperature, exceeding 600 K. Here, we discuss the metallization of high-quality epitaxial, smooth films of LFO on STO which we find results from a complex interplay of cation intermixing limited to one or two unit cells at the LFO/STO interface, and small amounts of oxygen off-stoichiometry. Moreover, using ionic liquid gating we find that we can tune STO/LFO heterojunctions reversibly between metallic and insulating states that is consistent with the controlled migration of oxygen from electric fields at the ionic liquid/LFO interface.

LFO films were grown by oxygen plasma assisted molecular beam epitaxy (MBE) in a deposition chamber with a base pressure of 10<sup>−10</sup> mbar on STO (SrTiO<sub>3</sub>) (001) substrates that were prepared in two distinct ways. In both cases, the substrates were TiO<sub>2</sub> terminated. In each case, the substrates underwent sequential cleaning with acetone, methanol, and deionized water, in an ultrasonic bath, each for 15 min, followed by dipping in 1:7 buffered hydrofluoric acid (BHF) with NH<sub>4</sub>F for ≈28 s to etch away the surface SrO layer.<sup>[25]</sup> Next, the STO substrates were rinsed in deionized water to remove residual BHF, and then dried in hot nitrogen gas. These STO substrates are referred to as type A substrates while those STO substrates that underwent an additional annealing procedure in a tube furnace at 1000 °C in flowing oxygen at a pressure of greater than 1 atm for 90 min are referred to as type B. For both type A and B substrates the surfaces are atomically smooth with terraces due to the vicinal miscut. Typical atomic force microscopy (AFM) images are shown in **Figure 1a,b** with corresponding 1D step height profiles measured perpendicular to the terrace direction shown in **Figure 1c,d**, respectively. In both cases, the step height is ≈3.9 Å, corresponding to one STO u.c. There are clear differences in the surface morphology with rougher terrace edges and terrace surfaces for type A substrates. The annealed substrates show atomically smooth terrace surfaces and edges. LaFeO<sub>3</sub> films were grown at 760 °C in an oxygen pressure of 4 × 10<sup>−7</sup> mbar (see the Experimental Section for more details) at a typical rate of ≈140 s u.c.<sup>−1</sup>. The surface morphology of the deposited LFO layers was similar to that of the corresponding STO substrates.

**Figure 1e** shows a typical time evolution of the intensity of the specularly reflected electron beam during reflection high-energy electron diffraction (RHEED) measurements of the growth of a typical LFO film on STO. The observed RHEED intensity oscillations are characteristic of 2D epitaxial layer-by-layer growth.<sup>[26]</sup> Each successive peak corresponds to the

Dr. P. Xu, Dr. W. Han, Dr. P. M. Rice,  
Dr. J. Jeong, Dr. M. G. Samant,  
Prof. S. S. P. Parkin  
IBM Research - Almaden  
650 Harry Road, San Jose, CA 95120, USA  
E-mail: stuart.parkin@icloud.com,  
stuart.parkin@mpi-halle.mpg.de



Dr. K. Mohseni, Dr. H. L. Meyerheim, Dr. S. Ostanin,  
Dr. I. Mertig, Prof. E. K. U. Gross, Dr. A. Ernst,  
Prof. S. S. P. Parkin  
Max Planck Institute for Microstructure Physics  
Weinberg 2, 06120 Halle, Germany  
Dr. I. V. Maznichenko, Dr. I. Mertig  
Institut für Physik  
Martin-Luther-Universität Halle-Wittenberg  
D-06099 Halle, Germany

DOI: 10.1002/adma.201604447

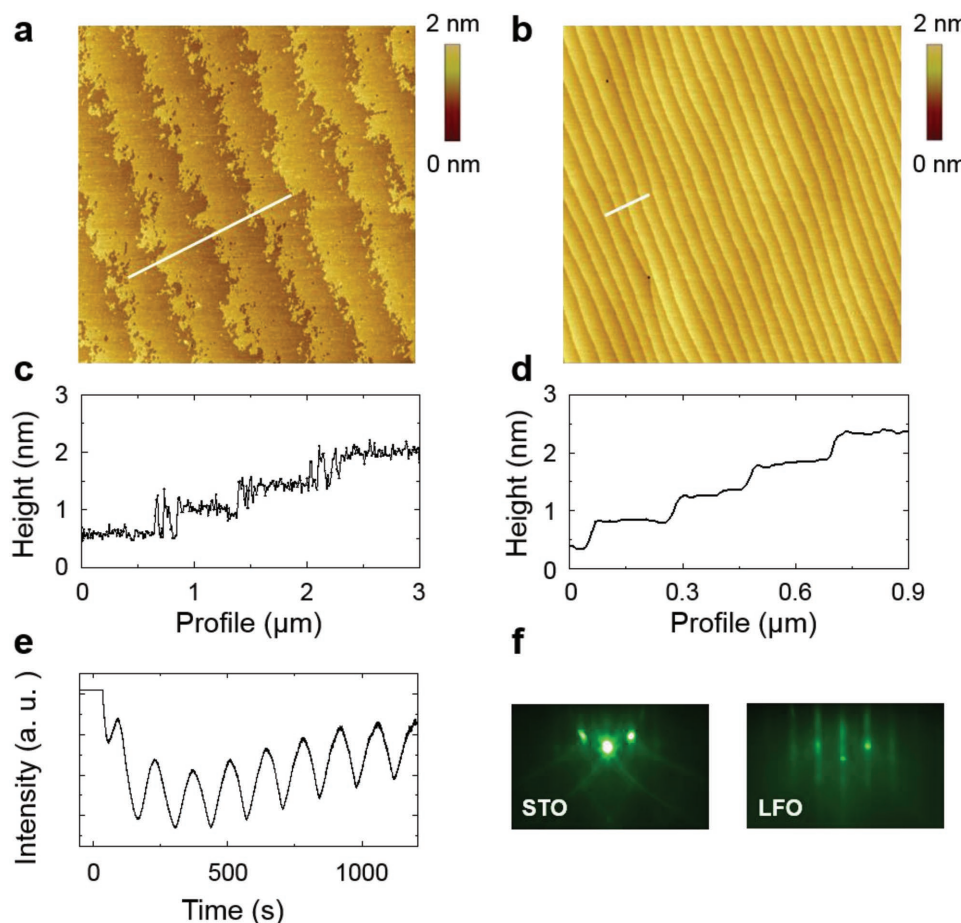


**Figure 1.** Characterization of STO substrate and LFO thin film AFM images of STO (001) and height profiles along the marked lines. a) AFM image of STO (001) subject to BHF etching, without annealing (type A substrate). b) AFM image of STO (001) after BHF etching and annealing (type B substrate). c,d) Height profile along the marked lines in (a) and (b), respectively. e) Typical RHEED specular spot intensity oscillation during deposition of LFO on STO. f) RHEED pattern from STO substrate prior to LFO growth (left) and after deposition of 20 u.c. of LFO.

growth of one u.c. of LFO which was confirmed by Rutherford backscattering (RBS). The RHEED oscillations were observed for more than 100 u.c. for substrates of both types. Moreover, the RHEED patterns for all LFO films grown for this study were streaky, thereby indicating the growth of smooth, epitaxial layers (Figure 1f). The composition of the LFO films, which could accurately be determined by RBS only for films with thicknesses  $\gg 100$  unit cells, had an atomic ratio of La to Fe of close to 1:1. X-ray diffraction (XRD) was used to determine the out-of-plane lattice parameter of the LFO layers, which was close to that of bulk LFO. Kiessig fringes (see the Supporting Information) associated with the LFO (002) XRD peak were consistent with the thickness of LFO layers determined from RHEED and RBS studies.

The sheet resistance ( $R_S$ ) of the LFO films was measured using a four-point inline probe method with contacts made from 25  $\mu\text{m}$  aluminum wires that were ultrasonically bonded directly to the surface of the LFO films. The distance between the contacts was much smaller than the sample size (10 mm  $\times$  10 mm). **Figure 2a** shows the dependence of  $R_S$  at room temperature on the LFO film thickness grown on type A substrates. LFO films with thicknesses below 2 u.c.

were insulating with resistance out of the measurement range of our instrument ( $>10^9 \Omega \square^{-1}$ ). As the thickness of the LFO layer,  $t$ , was increased above 3 u.c., the resistance dropped and reached a constant value of  $\approx 16 \text{ k}\Omega \square^{-1}$  for  $t > 20$  u.c. By contrast the sheet resistance of LFO films grown on type B substrates was always too high to be measured irrespective of the LFO thickness (see inset to Figure 2a).

Detailed electrical properties, including sheet resistance, carrier density, and mobility, for the blanket LFO films were measured using the Van der Pauw method (Figure 2b–d).<sup>[27]</sup> Electrical contacts of ruthenium and gold bilayers (5 nm Ru/65 nm Au) were deposited by ion-beam deposition at the four corners of the substrate using a metal shadow mask. Temperature-dependent measurements were carried out in a Quantum Design physical property measurement system (PPMS). Typical  $R_S(T)$  curves for samples with thicknesses of 4, 6, and 90 u.c. are shown in Figure 2b. (Note that the measurements at room temperature are in good agreement with the four-point inline measurements). For  $t \leq 3$  u.c. the samples display an insulating behavior, while samples with  $t \geq 4$  u.c. are metallic. Thus, we find evidence for an insulator-to-metal transition with increasing LFO thickness at room temperature

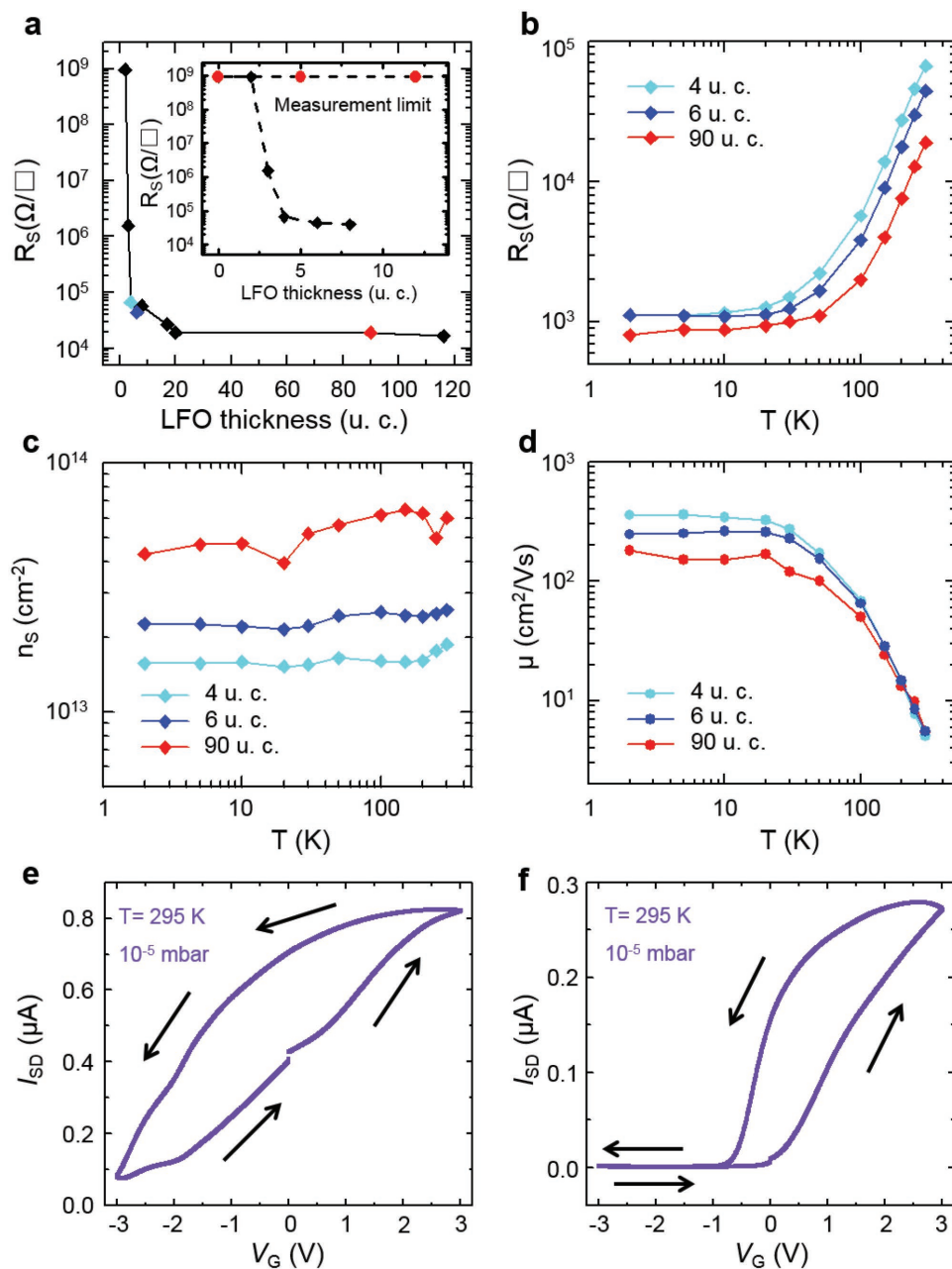


**Figure 2.** Transport property of the LFO/STO interface for LFO grown on STO substrates. a) LFO thickness dependent room temperature sheet resistance. Inset: Comparison of room temperature sheet resistance of the interface for LFO grown on STO substrates of type A (black) and type B (red). Temperature dependence of b) sheet resistance, c) carrier density, and d) mobility of the heterointerface between LFO and  $\text{TiO}_2$ -terminated STO of type A. Source–drain current versus gate voltage for 4 u.c. LFO grown on e) type A and f) type B STO.

for type A STO substrates. The charge carriers are determined to be of electron character by the van de Pauw Hall measurements. At room temperature the carrier density for these samples is  $\approx 1.9 \times 10^{13}$ ,  $\approx 2.6 \times 10^{13}$ , and  $\approx 6.0 \times 10^{13} \text{ cm}^{-2}$ , respectively. The thickness dependence of the carrier density shows that the carriers are confined close to the STO/LFO interface. The carrier density varies weakly with temperature, as shown in Figure 2c but, on the other hand, the electron mobility increases significantly upon cooling reaching values of  $\approx 180$ ,  $\approx 246$ , and  $\approx 355 \text{ cm}^2 \text{ V}^{-1} \text{ s}^{-1}$  at 2 K for the 90, 6, and 4 u.c.

thick films, respectively (Figure 2d). Interestingly, the thinner layers show higher mobilities, consistent with an electron gas at the interface. One way to rationalize this is that the larger carrier density ( $n_s$ ) in the thicker films (see Figure 2c) results in an increased scattering rate (e.g., electron–electron, electron–phonon), corresponding to a larger effective electron mass. Since the carrier mobility is inversely proportional to the effective mass, its value decreases as the film thickness is increased.

To ensure that the metallicity found for type A LFO films derives from the deposited LFO layer, we measured the

electrical properties of a type A STO (001) substrate that was subjected to exactly the same sequence of temperature and oxygen pressure conditions, including the identical operation of the La and Fe evaporation cells (but with the shutters kept closed) that was used during the LFO growth. This control sample was insulating at room temperature, thereby indicating that the conducting state is not due to the creation of defects within the STO substrate: it is well known that oxygen vacancies can give rise to conducting STO (001) surfaces.<sup>[28,29]</sup> To rule out the possibility that the observed conductivity is an inherent property of the LFO film, we grew LFO films of thicknesses 20 and 25 u.c. on LaAlO<sub>3</sub> (LAO) (001) substrates, and on 1 u.c. SrO capped type A STO (001) substrates using the same growth conditions for growth on TiO<sub>2</sub>-terminated STO (001). In both cases, the LFO films were insulating (see the Supporting Information for details). These results indicate that the conductivity of the type A LFO films arises from the STO/LFO interface.

First principles calculations of an ideal LFO/TiO<sub>2</sub>-terminated STO interface without any cation intermixing or oxygen vacancies indicate the formation of a 2DEG irrespective of the LFO thickness (see Figure 3). This prediction and the absence of any metallicity for LFO films grown on type B STO are difficult to reconcile with these calculations, most likely due to imperfect interfaces. We first consider the possibility of cation intermixing which can be probed using atomic resolution, cross-sectional scanning transmission electron microscope (STEM), and electron energy loss spectroscopy (EELS).

High-angle annular dark field (HAADF) scanning transmission electron microscopy (STEM) images of the interfaces of both conducting (Figure 4a, 21 u.c. LFO on type A STO) and insulating (Figure 4b, 12 u.c. LFO on type B STO) samples indicate excellent lattice matching between LFO and STO with no dislocations. This is not surprising as the lattice mismatch between LFO and STO is only ≈0.53%. The EELS data obtained in the rectangular region marked in Figure 4a,b are used to derive the elemental maps that are shown in Figure 4c,d, respectively. Away from the interface the EELS data show clear layer-by-layer oscillations in concentrations of the respective elements that are consistent with alternating layers of (LaO)<sup>1+</sup> and (FeO<sub>2</sub>)<sup>1-</sup>, and (SrO) and (TiO<sub>2</sub>), expected for ideal LFO (001) and STO (001), respectively. Thus, the crystal quality of the LFO layer and its interface with STO is very good and comparable to the highest quality oxide interfaces grown on STO (001).<sup>[30]</sup> Nevertheless, the EELS data do suggest some cation intermixing within one or two unit cells of the STO/LFO interface. As can be seen in Figure 4c,d the

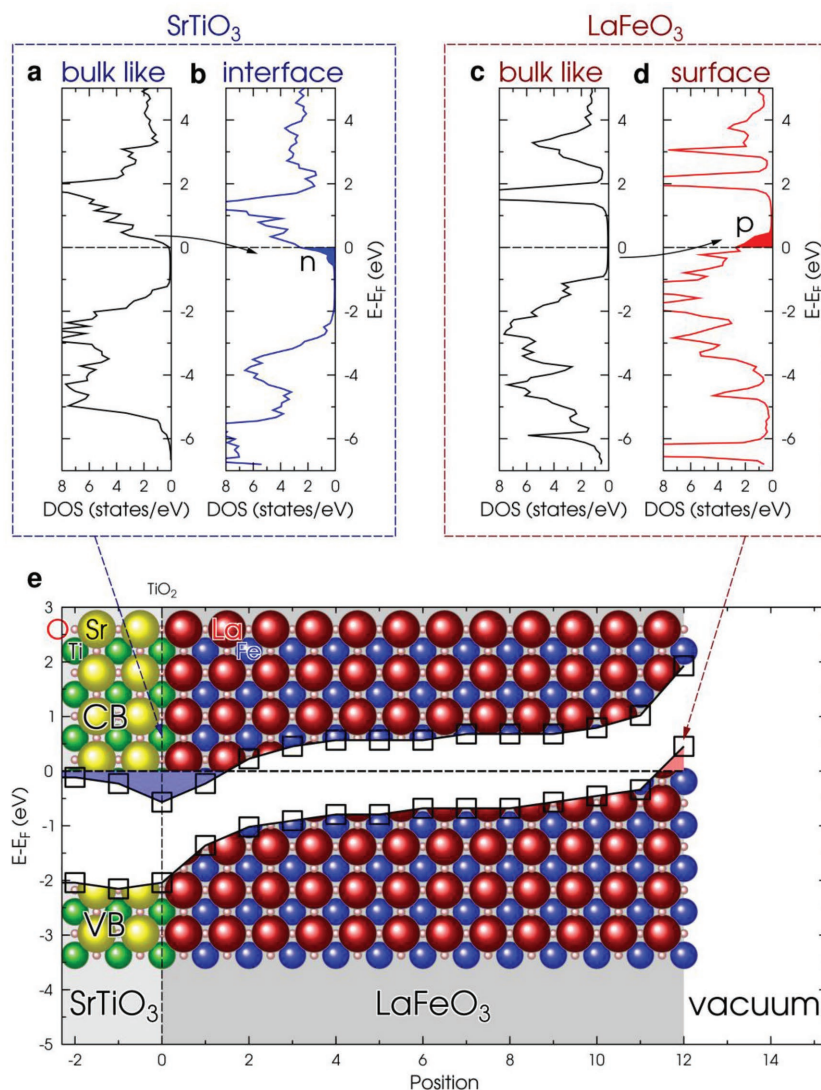


**Figure 3.** Layer-resolved bandgap and the density of states close to the Fermi level in an ideal LFO thin film on the STO (001) substrate. The upper panels show the density of states of the STO bulk (a) and interface (b) and the LFO bulk (c) and surface (d). Lower panel (e) presents the 2DEG and 2D hole gas formation: 2DEG is found at the TiO<sub>2</sub>-terminated LFO/STO interface, while 2D hole gas is formed at the FeO<sub>2</sub>-terminated LFO surface.

columns of atoms in both substrate types at the interface are neither pure Sr (yellow) nor pure La (red), but are a mixture of these two elements. The EELS line profiles shown in Figure 4e,f indicate that the cation intermixing at the interface is more pronounced for the insulating sample (type B). We made STEM measurements on seven samples, five insulating (type B), and two conducting (type A) and all showed a similar lack of atomically abrupt interfaces with cation intermixing.

One likely reason for the increased cation mixing that we observe for the type B samples with smoother surfaces is the higher mobility of atoms as compared to the case of the corrugated interface in type A samples. At a corrugated interface a cation is more likely to be trapped at steps or other imperfections (see Figure 1c). The annealing process leads to an overall smoothing of the surface by removal of structural

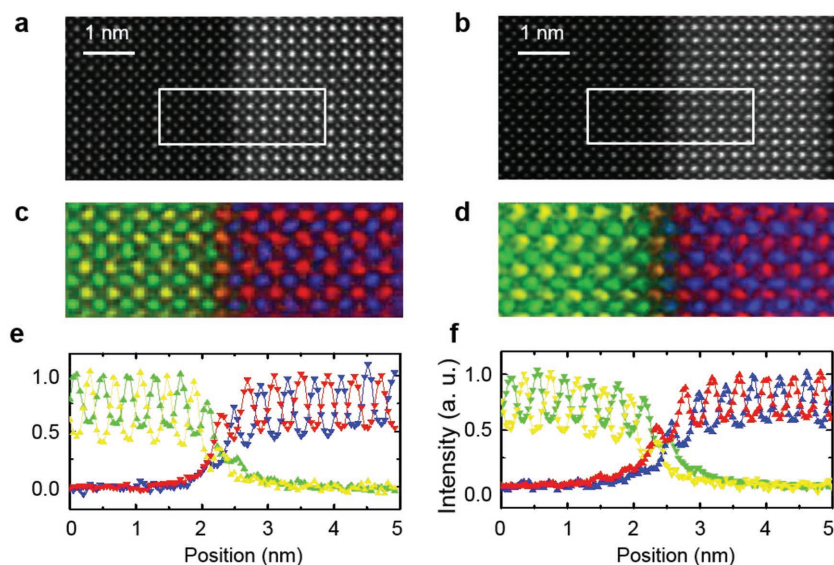


**Figure 4.** STEM results of the interface between LFO and STO. a) Atomic-resolution HAADF-STEM image of 21 u.c. LFO grown on substrate of type A which was taken along the [100] zone axis. The growth direction is from left to right. c) Electron energy loss spectroscopy map acquired from the rectangular area in (a) (10 nm  $\times$  5 nm), with a 0.5 Å step size and a dwell time of 10 ms. The green is Ti, the yellow is Sr, the blue is Fe, and the red is La. e) The position-dependent normalized elemental profile plots. b,d,f) The STEM results of a 12 u.c. LFO grown on substrate of type B [(b), (d)] with 0.33 Å step size and a dwell time of 2 ms].

defects. Consequently, on a smoother surface less atoms are trapped at these structural defects and possess sufficient energy to overcome the activation barrier for the cation exchange process.

Surface X-ray diffraction (SXRD) experiments were undertaken to probe the LFO/STO interface structure with higher precision. Two samples with 6 u.c. thick LFO layers on types A and B substrates were probed by collecting the intensity distribution along the integer order crystal truncation rods (CTRs) (see the Supporting Information for details). Owing to the high symmetry (plane group  $p4mm$ ) of the crystal structure these data needed to be fit by  $z$  parameter, an overall Debye parameter describing static and dynamic disorder, and the occupancy factors ( $\Theta$ ) of the atomic species within each layer. While atomic relaxations were not found to be significant at the interface there was significant chemical roughness characterized by a cationic intermixing between  $\text{La}^{3+}$  and  $\text{Sr}^{2+}$  by diffusion of La atoms into the SrO layer. This  $\text{La}^{3+}$  and  $\text{Sr}^{2+}$  intermixing is determined to be 25% for the insulating sample (type B), but only at most 10% for the conducting sample (type A). While the cationic intermixing between  $\text{La}^{3+}$  and  $\text{Sr}^{2+}$  can be determined accurately, the determination of the Fe/Ti intermixing is inherently less accurate due to the low  $z$  contrast between the scattering amplitudes of Fe and Ti (see the Supporting Information). **Figure 5a,c** shows the SXRD derived model of the interface structure (see the Supporting Information).

Recently, we have shown that ionic liquid (IL) gating can be used to control the oxygen vacancy concentration at the surface of STO (001)<sup>[31]</sup> and deep within the bulk of oxide films that have volume channels that allow for oxygen migration induced by electric fields created at the surface of the oxide layer with

the ionic liquid.<sup>[32–35]</sup> Hence, we use IL gating to probe the presence or lack of oxygen vacancies at LFO/STO interface in the two types of substrates. Lateral three-terminal field effect transistor devices with an ionic liquid gate dielectric were fabricated from 4 u.c. thick LFO films deposited on types A and B substrates by standard photolithography techniques.<sup>[32]</sup> For the insulating type B sample the device channel was defined by lift-off techniques within a 60 nm thick dielectric  $\text{SiO}_2$  that was deposited on top of the STO/LFO film. For the conducting type A sample, the film outside the channel was first ion milled to thin the LFO layer to less than a thickness of 3 u.c. to make it insulating, and then refilled with a 60 nm thick layer of insulating  $\text{SiO}_2$ . Consistent with this process devices on the same wafer were determined to be electrically isolated from each other. The channel for both sets of devices had a size of 900  $\mu\text{m} \times$  300  $\mu\text{m}$ .

All gating experiments were carried out on devices having a Hall bar geometry at room temperature with a source–drain voltage of 100 mV. **Figure 2e,f** shows the source–drain current ( $I_{\text{SD}}$ ) versus gate voltage ( $V_{\text{G}}$ ) curve measured at a ramp rate of 5  $\text{mV s}^{-1}$  in a vacuum chamber at a pressure of  $1 \times 10^{-5}$  mbar for two devices A and B, corresponding to substrates types A and B with 4 u.c. thick LFO layers. The most important result is that both devices could be reversibly switched between high and low resistance states by sweeping  $V_{\text{G}}$ . Thus, the insulating and metallic states could be accessed in both cases by IL gating consistent with the metallic states being formed from the presence of oxygen vacancies (see the Supporting Information). Although the metallic and insulating states of the STO/LFO films on types A and B substrates are stable in air the metallic state of device A can be made much more resistive by reverse gating in oxygen (see the Supporting Information). Even for the case of thinner films (<3 u.c.) the samples could be metallized by ionic liquid gating: **Figure S6** (Supporting Information) shows the metallization of a 2 u.c. thick LFO film on a type A substrate.

Given the experimental evidence for both cation intermixing at the STO/LFO interface and variations from the ideal oxygen stoichiometry we have carried out first principles calculations of the electronic structure that includes such imperfections. The crystalline structure and the chemical composition obtained from the SXRD experiments for samples of types A and B were used as the initial basis for these calculations (**Figure 5a,d**). Remarkably, these calculations find that the type A sample is conducting and the type B sample is insulating in agreement with our experimental measurements. Compared to the ideal interface case that we mentioned earlier, the density of states at the Fermi level is calculated to be smaller in the imperfect type A sample than for the ideal case. It is not surprising that deviations from the ideal interface would strongly affect the electronic properties, and thus the transport properties, of the interface.

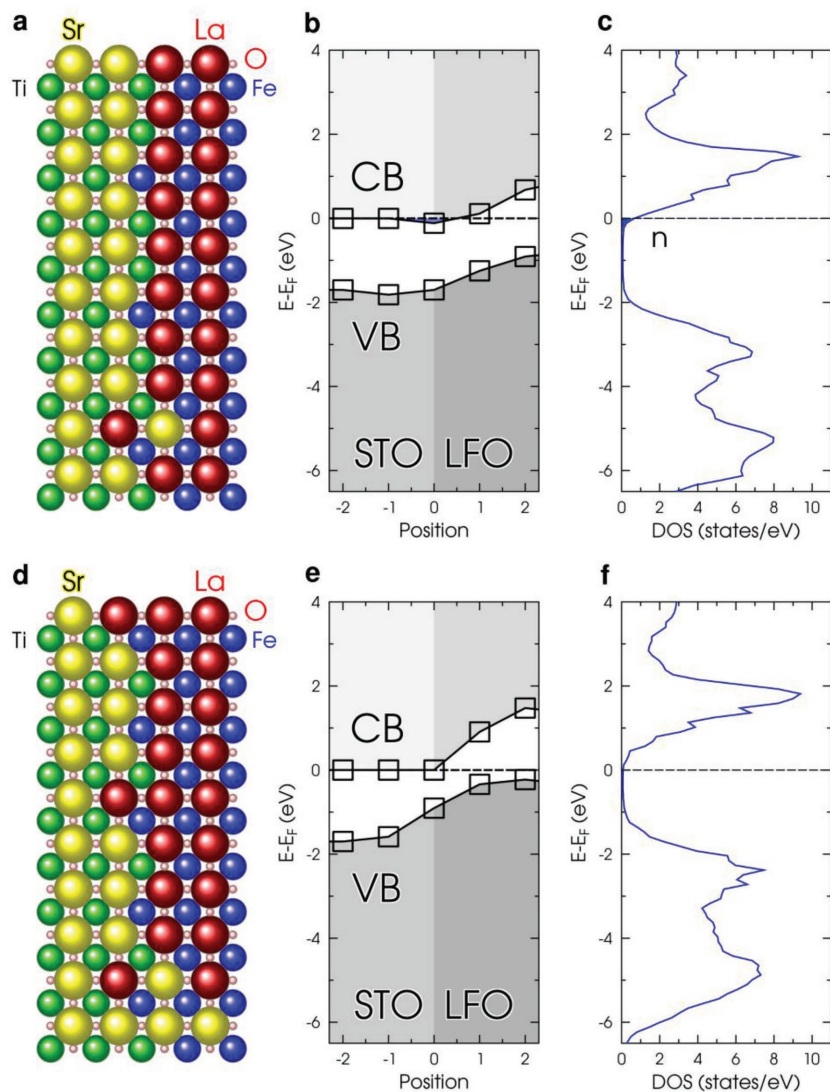


**Figure 5.** Layer-resolved bandgap and the density of states close to Fermi level. Results for samples of the type A (upper panel) and type B (lower panel). a, d) Schematic of the crystal-line information and the occupation of atomic sites adopted from the SXRd experiment (see Figure S8, Supporting Information, for more details). The position of the interface is at 0. SXRd experiments provide evidence for cationic intermixing of  $\text{Sr}^{2+}$  versus  $\text{La}^{3+}$  and  $\text{Fe}^{3+}$  versus  $\text{Ti}^{4+}$ . a) Representative for the conducting sample, for which a 10% cationic  $\text{Sr}^{2+}/\text{La}^{3+}$  and 25%  $\text{Fe}^{3+}/\text{Ti}^{4+}$  intermixing is found. d) The insulating sample has a 25% cationic  $\text{Sr}^{2+}/\text{La}^{3+}$  and about 50%  $\text{Fe}^{3+}/\text{Ti}^{4+}$  exchange. b, e) The layer-resolved change of the bandgap in the conducting and insulating samples, respectively. c, f) The corresponding densities of states at the interface.

We considered the following types of defects and imperfections: oxygen deficiency and excess, cation vacancies, La/Sr and Fe/Ti diffusion at the  $\text{TiO}_2$ -terminated interface in accordance with our experimental findings. In general, we found that La and Ti vacancies, the cation intermixing (La for Sr and Fe for Ti) reduces the density of states close to the Fermi level (p-doping) and opens the bandgap, while oxygen vacancies are n-doping and favor the 2DEG formation (see Figure S9–S14, Supporting Information). The LFO films thickness and the defect density influence the impact of the defects on the 2DEG. So, for 2 u.c. thick LFO film the La/Sr intermixing of 10% at the LFO/STO interface restores the bandgap, while the interface remains

conducting for the same intermixing in 4 u.c. thick LFO film, although the width of the density of states at the Fermi level is getting smaller than that in the perfect interface case. This explains our experimental finding that the interface is insulating below the critical thickness of 3 u.c. where a small amount of cation intermixing leads to the insulating state. The same effect happens if the  $\text{TiO}_2$ -terminated STO surface is annealed under the oxygen pressure before the LFO deposition (type B). In this case, the STO/LAO interface can be oxygen rich (with oxygen in interstitial positions), which act as p-dopants and reduce significantly electron charge carriers. In addition, the annealing smoothens out the interface boundaries (Figure 1) and favors the cation intermixing, which suppresses the 2DEG formation in accordance with our simulations.

In summary, we observe the presence or absence of a 2DEG at an interface between LFO(001) and STO(001), for LFO layers above a critical thickness of  $\approx 3$  u.c., which STEM and SXRd show is nearly ideal, namely, epitaxial and atomically smooth, in both cases. The ideal interface we calculate should display a 2DEG, independent of the LFO thickness. From detailed experimental studies and theoretical models we show that the 2DEG is a result of a complex interplay between cation intermixing in 1–2 interface layers and oxygen vacancies in the same layers. We show that ionic liquid gating can, through changes in the oxygen vacancy concentration, control the presence of the 2DEG. Our results are very interesting for the field of oxide electronics<sup>[3,6]</sup> in understanding the origin of 2DEG at oxide interfaces.

## Experimental Section

**Substrate Preparation:** Substrates were chemically cleaned, as discussed in the main text. Type B substrates were subject to a high-pressure oxygen anneal. The anneal was carried out in flowing oxygen (100 sccm) in a partially sealed tube furnace. The substrate was inserted into the cold furnace, heated at  $15\text{ }^\circ\text{C min}^{-1}$  to  $1000\text{ }^\circ\text{C}$ , soaked for 90 min, and cooled in flowing  $\text{O}_2$  at  $5\text{ }^\circ\text{C min}^{-1}$  to  $<300\text{ }^\circ\text{C}$  before removal from the furnace into air. The substrate was then characterized by AFM before insertion into the deposition system.

**Sample Growth:**  $\text{LaFeO}_3$  films were grown at  $760\text{ }^\circ\text{C}$  by an oxygen plasma assisted MBE in a system with a base pressure of  $10^{-10}$  mbar. The deposition geometry consisted of a single cluster of La, Sr, and Fe thermal evaporation cells and an oxygen rf plasma source all pointing to the substrate at an incidence angle of  $7^\circ$  from the substrate normal. The temperatures of evaporation cells of La, Sr, and Fe were  $1290$ ,  $530$ , and  $1260\text{ }^\circ\text{C}$ , respectively. During growth the substrate was rotated and positioned above the cell cluster at a distance of  $\approx 40.2$  cm. The RHEED studies (differential pumping was not used or needed) were performed

without sample rotation at a deposition distance of  $\approx 49.4$  cm. The transport properties of LFO films grown at either height were identical. The STO substrates were heated and cooled at a ramp rate of  $25\text{ }^\circ\text{C min}^{-1}$  in the MBE chamber. The oxygen rf plasma source was operated with an oxygen flow rate of 4 sccm such that the chamber oxygen pressure was maintained at  $4 \times 10^{-7}$  mbar during heating cooling of the substrates and during  $\text{LaFeO}_3$  growth. The plasma was maintained when the substrate temperature exceeded  $\approx 300\text{ }^\circ\text{C}$ .

**Electrical Transport Measurements:** Two methods were used to measure the sheet resistance of the films in this study. The first method was a four-point inline technique that relied on ultrasonic bonding of Al wires to the sample. This method punches a hole in the film and makes direct contact to the buried interfaces. A second method was a van der Pauw technique that used shadow-masked Ru/Au bilayer contacts that were deposited at the four corners of the square substrates. The substrate holder used during LFO deposition masked these four corners so that there was no LFO film deposited at these corners. Thus, the Ru/Au bilayer electrically contacted the edge of the LFO film including the LFO/STO interface. Moreover, the sheet resistance measured by both these techniques was comparable for all films.

**STEM and EELS Measurements:** The JEOL ARM 200F with a Cold-FEG source was operated at 200 keV. The EELS signal was recorded on a GIF Quantum 965 with Dual EELS option. The usual conditions for EELS mapping use a 200 pA beam with a beam convergence semiangle of  $30.7$  mrad and an EELS collection semiangle of  $112$  mrad. The EELS maps were subjected to a principal component noise reduction analysis called MSA from HREM Research Inc. The elemental maps were created by integrating the signals over various windows: 50 eV for Ti, 75 eV for Fe and La, and 200 eV for Sr. The maps were smoothed and then sharpened using the available Digital Micrograph pull downs and added together using the Color mix pallet. The EELS maps (Figure 4c,d) were converted into normalized profile plots (Figure 4e,f) by selecting the EELS integrated signal data for each element in rows three pixels wide, centered on each element's atomic rows, summing them, and dividing by the average of their peak values. For example, the green line in the profile Figure 4e is the normalized sum of 12 rows of data from Figure 4c centered on the four Ti rows. The same was done for the map Figure 4d except the increased spatial resolution allowed to use rows four pixels wide. For example, the green line in profile Figure 4f is the normalized sum of 16 rows of data centered on the four Ti rows.

**SXRD Measurements:** The SXRD experiments were carried out at the beamline ID03 of the European Synchrotron Radiation Facility (ESRF) in Grenoble, France, using a six circle ultrahigh vacuum diffractometer operated in the Z-axis mode. X-ray intensity data were collected using a 2D Maxipix detector at grazing incidence ( $\alpha_i = 2^\circ$ ) of the incoming X-ray beam of 24 keV. For each datum set six symmetry independent crystal truncation rods ( $\approx 700\text{--}800$  reflections in total) were collected up to a maximum momentum transfer of  $q_z = 3.7$  reciprocal lattice units.

**Device Fabrication and Ionic Liquid Gating Experiments:** After defining the channel by standard photolithography techniques, ohmic contacts were made by depositing 5 nm Ru and 65 nm Au in a Hall bar geometry for electrical measurements. To prevent the interaction of gold with IL, all exposed gold surface other than the electrode pad area outside the channel were covered with 60 nm  $\text{SiO}_2$ . Finally, a  $1000\text{ }\mu\text{m} \times 1000\text{ }\mu\text{m}$  gate pad was formed from a trilayer of 60 nm  $\text{Al}_2\text{O}_3/5\text{ nm Ru}/65\text{ nm Au}$  that was spaced  $\approx 250\text{ }\mu\text{m}$  from one side of the channel. An organic IL, 1-hexyl-3-methylimidazolium bis(trifluoromethylsulfonyl)-imide (HMIM-TFSI, EMD Chemicals), was used in these studies. Before the gating experiment, both IL and sample were baked in high vacuum at  $120\text{ }^\circ\text{C}$  for at least 8 h, to remove any residual water in the system. Next, a droplet of the dehydrated IL was placed on the device such that it covered both the channel and the gate electrode. The sample was then transferred immediately to a high vacuum chamber for gating experiments.

**First Principles Calculations:** The experimentally obtained structural information was used for calculations of the electronic and magnetic properties of LFO/STO interfaces using a self-consistent full-charge Green function method within the density functional theory, which is specially designed for semi-infinite systems.<sup>[36]</sup>

## Supporting Information

Supporting Information is available from the Wiley Online Library or from the author.

## Acknowledgements

The authors gratefully acknowledge Chris Lada for help with the design and construction of the MBE, Kevin Roche for technical assistance, Leslie E. Thompson and Erik Larafor for TEM sample preparation, and Andrew Kellock for performing RBS measurements. This work was supported by the DFG through SFB 762.

Received: August 20, 2016

Revised: October 5, 2016

Published online:

- [1] E. Dagotto, Y. Tokura, *Mater. Res. Bull.* **2008**, *33*, 1037.
- [2] B. Keimer, J. Maier, J. Mannhart, *Nat. Mater.* **2012**, *11*, 751.
- [3] J. Mannhart, D. G. Schlom, *Science* **2010**, *327*, 1607.
- [4] C. Noguera, *J. Phys.: Condens. Matter* **2000**, *12*, R367.
- [5] H. Y. Hwang, Y. Iwasa, M. Kawasaki, B. Keimer, N. Nagaosa, Y. Tokura, *Nat. Mater.* **2012**, *11*, 103.
- [6] J. Mannhart, D. H. A. Blank, H. Y. Hwang, A. J. Millis, J.-M. Triscone, *Mater. Res. Bull.* **2008**, *33*, 1027.
- [7] S. Stemmer, S. J. Allen, *Annu. Rev. Mater. Res.* **2014**, *44*, 151.
- [8] A. Ohtomo, H. Y. Hwang, *Nature* **2004**, *427*, 423.
- [9] S. Thiel, G. Hammerl, A. Schmehl, C. W. Schneider, J. Mannhart, *Science* **2006**, *313*, 1942.
- [10] C. Cen, S. Thiel, J. Mannhart, J. Levy, *Science* **2009**, *323*, 1026.
- [11] M. Huijben, G. Rijnders, D. H. A. Blank, S. Bals, S. V. Aert, J. Verbeeck, G. V. Tendeloo, A. Brinkman, H. Hilgenkamp, *Nat. Mater.* **2006**, *5*, 556.
- [12] S. Okamoto, A. J. Millis, *Nature* **2004**, *428*, 630.
- [13] Y. Hotta, T. Susaki, H. Y. Hwang, *Phys. Rev. Lett.* **2007**, *99*, 236805.
- [14] P. Perna, D. Maccariello, M. Radovic, U. Scotti di Uccio, I. Pallicchi, M. Codda, D. Marré, C. Cantoni, J. Gazquez, M. Varela, S. J. Pennycook, F. M. Granozio, *Appl. Phys. Lett.* **2010**, *97*, 152111.
- [15] P. Moetakef, T. A. Cain, D. G. Ouellette, J. Y. Zhang, D. O. Klenov, A. Janotti, C. G. Van de Walle, S. Rajan, S. J. Allen, S. Stemmer, *Appl. Phys. Lett.* **2011**, *99*, 232116.
- [16] J. Biscaras, N. Bergeal, S. Hurand, C. Grossetête, A. Rastogi, R. C. Budhani, D. LeBoeuf, C. Proust, J. Lesueur, *Phys. Rev. Lett.* **2012**, *108*, 247004.
- [17] C. A. Jackson, J. Y. Zhang, C. R. Freeze, S. Stemmer, *Nat. Commun.* **2014**, *5*, 4258.
- [18] S. A. Chambers, *Surf. Sci.* **2011**, *605*, 1133.
- [19] G. Herranz, M. Basletic, M. Bibes, C. Carrétéro, E. Tafr, E. Jacquet, K. Bouzehouane, C. Deranlot, A. Hamzic, J.-M. Broto, A. Barthélémy, A. Fert, *Phys. Rev. Lett.* **2007**, *98*, 216803.
- [20] A. Kalabukhov, R. Gunnarsson, J. Borjesson, E. Olsson, T. Claeson, D. Winkler, *Phys. Rev. B* **2007**, *75*, 121404.
- [21] J. N. Eckstein, *Nat. Mater.* **2007**, *6*, 473.
- [22] Z. Q. Liu, C. J. Li, W. M. Lü, X. H. Huang, Z. Huang, S. W. Zeng, X. P. Qiu, L. S. Huang, A. Annadi, J. S. Chen, J. M. D. Coey, T. Venkatesan, Ariando, *Phys. Rev. X* **2013**, *3*, 021010.
- [23] Y. Chen, N. Pryds, J. e. E. Kleibeuker, G. Koster, J. Sun, E. Stamaté, B. Shen, G. Rijnders, S. Linderoth, *Nano Lett.* **2011**, *11*, 3774.
- [24] M. Eibschütz, S. Shtrikman, D. Treves, *Phys. Rev.* **1967**, *156*, 562.
- [25] M. Kawasaki, K. Takahashi, T. Maeda, R. Tsuchiya, M. Shinohara, O. Ishiyama, T. Yonezawa, M. Yoshimoto, H. Koinuma, *Science* **1994**, *266*, 1540.

- [26] W. F. Egelhoff, I. Jacob, *Phys. Rev. Lett.* **1989**, 62, 921.
- [27] L. J. van der Pauw, *Philos. Res. Rep.* **1958**, 20, 220.
- [28] C. S. Koonce, M. L. Cohen, J. F. Schooley, W. R. Hosler, E. R. Pfeiffer, *Phys. Rev.* **1967**, 163, 380.
- [29] D. W. Reagor, V. Y. Butko, *Nat. Mater.* **2005**, 4, 593.
- [30] D. A. Müller, L. F. Kourkoutis, M. Murfitt, J. H. Song, H. Y. Hwang, J. Silcox, N. Dellby, O. L. Krivanek, *Science* **2008**, 319, 1073.
- [31] M. Li, T. Graf, T. D. Schladt, X. Jiang, S. S. P. Parkin, *Phys. Rev. Lett.* **2012**, 109, 196803.
- [32] J. Jeong, N. Aetukuri, T. Graf, T. D. Schladt, M. G. Samant, S. S. P. Parkin, *Science* **2013**, 339, 1402.
- [33] J. Jeong, N. B. Aetukuri, D. Passarello, S. D. Conradson, M. G. Samant, S. S. P. Parkin, *Proc. Natl. Acad. Sci. USA* **2015**, 112, 1013.
- [34] S. G. Altendorf, J. Jeong, D. Passarello, N. B. Aetukuri, M. G. Samant, S. S. P. Parkin, *Adv. Mater.* **2016**, 28, 5284.
- [35] D. Passarello, S. G. Altendorf, J. Jeong, M. G. Samant, S. S. P. Parkin, *Nano Lett.* **2016**, 16, 5475.
- [36] M. Lüders, A. Ernst, W. M. Temmerman, Z. Szotek, P. J. Durham, *J. Phys.: Condens. Matter* **2001**, 13, 8587.